

Flow-destabilized seiches in a reservoir with a movable dam

I. J. HEWITT¹†, H. SCOLAN² AND N. J. BALMFORTH¹

¹Department of Mathematics, University of British Columbia, Vancouver, V6T 1Z2, Canada

²Laboratoire des Écoulements Géophysiques et Industriels (LEGI), CNRS-INPG-UJF,
BP 53X, 38041 Grenoble, France

(Received 17 March 2010; revised 4 February 2011; accepted 3 March 2011)

Using a combination of theoretical modelling and experiments, seiches in a reservoir are shown to become linearly unstable due to the coupling with flow under a dam that opens and closes in response to the upstream water pressure. The phenomenon is related to the mechanism commonly attributed to generate sound in musical instruments like the clarinet. Shallow water theory is used to model waves in the reservoir, and these are coupled, by an outflow condition, to a nonlinear oscillator equation for the dam opening. In general, several modes of oscillation are predicted to be unstable, and the frequency of the most unstable mode compares well with the dominant frequencies observed in the experiments. The experiments also show a systematic variation of the amplitude and spatial structure of the oscillations with the weight of the dam, reflecting the nonlinear coupling between the unstable modes of the system.

Key words: hydraulics, instability, wave–structure interactions

1. Introduction

In this paper, we explore an instability that arises in a simple hydraulic system due to fluid–structure interaction. The system consists of a reservoir dammed at one end by an obstruction that opens and closes in response to variations in upstream water pressure (figure 1). Flow through the reservoir can induce an instability in which the back and forth sloshing of fluid in the reservoir (i.e. a seiche) becomes coupled to vertical oscillations of the dam. The instability relies on the two coupled, component oscillators (the reservoir seiche and the rocking dam) exerting a positive feedback on one another, which becomes possible when the periods and phases of the two are suitably tuned.

The instability is analogous to that commonly thought to operate in woodwind instruments such as the clarinet, where air flow past a vibrating reed interacts with sound waves in an adjacent air column. The feedback between the oscillating reed and air column holds the key to generating sound, as first described by Helmholtz (1954). The hydrodynamic version of the process explored here provides a visible demonstration of this effect: the reservoir plays the role of the air column, and the dam plays the role of the reed. As far as we are aware, however, the stability properties of this simple hydraulic system have not previously been explored.

† Email address for correspondence: hewitt@math.ubc.ca

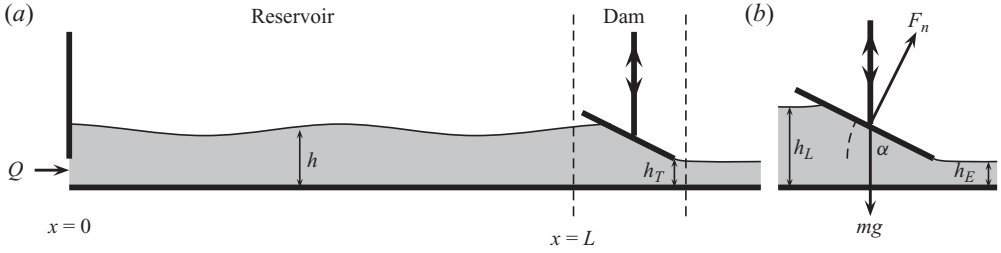


FIGURE 1. (a) Geometry of the model system. The dashed lines indicate the dam region of the model as shown in (b).

There have been a number of previous studies of flow-induced vibrations of sluice gates for engineering applications (e.g. Hardwick 1974; Kolkman 1977; Billeter & Staubli 2000). In these cases, the oscillations are most commonly associated with vortex shedding and instability of shear layers created by flow separation under the gate. In the system that we study, however, the dam is an angled plate from which the flow does not separate until it reaches the trailing edge (see figure 1); the oscillations are instead due to the interaction with waves in the upstream reservoir. The situation is more similar to some other river-gate oscillations (Bakker *et al.* 1991; Jongeling & Kolkman 1995) which resonate with standing ‘cross-waves’ established across the width of the channel. There are also related instabilities associated with unsteady flow through industrial valves (Weaver & Ziada 1980; Misra, Behdinan & Cleghorn 2002).

Destabilization by flow is the central component in a large number of fluid–structure interaction problems such as the operation of the vocal chords, the oscillations of bridges and the flutter of flags, sails and wings (Fitt & Pope 2000; Argentina & Mahadevan 2005; Mandre & Mahadevan 2009). In these particular flow instabilities, the oscillations are natural modes of the structure which are excited by the flow. Our hydraulic system, on the other hand, is destabilized by the coupling between a mode of the structure and one in the fluid, which places it into the type C category in the classification scheme suggested by Benjamin (1960) and Landahl (1962).

The most relevant previous work appears to be studies of the clarinet (Backus 1961, 1963; Wilson & Beavers 1974; McIntyre, Schumacher & Woodhouse 1983). In that instrument, the reed lies at the inlet of the air column, rather than the outlet, but apart from this distinction the physical mechanism for instability is very similar. The reed is generally treated as a damped linear oscillator that has a natural frequency much higher than the lowest frequency of the instrument. The player learns to control the air pressure with which to blow in order to excite modes closer to the natural frequencies of the air column rather than that of the reed. As has been shown both theoretically and experimentally, however, the coupling to the reed alters those natural frequencies. We find analogous results for the current problem, and that the coupling is fundamental in exciting the modes through an intrinsic instability.

The same type of instability may also operate in magmatic conduits, thereby generating the unsteady motions in the surrounding rock that may explain volcanic tremor (Julian 1994; Rust, Balmforth & Mandre 2008). In this scenario, magma sloshing in a long conduit interacts with flow through a tight constriction which opens and closes due to elastic deformation of the rock and varying magma pressure. Analogies have also been drawn to explain ‘singing icebergs’ (Müller *et al.* 2005), although that phenomenon has yet to be explored in any detail.

In §2, we describe our theory involving shallow water waves in a long reservoir, with the outflow regulated by the vertical position of the movable dam. Certain modes of oscillation, related to natural frequencies of the reservoir and the dam, are predicted to be linearly unstable. In §3, we describe the results of a simple experiment in which the dam is created by an angled plate, attached by an arm to a pivot further downstream. This arrangement, with the arm able to rotate in response to varying pressure on the plate, approximately recreates the theoretical setup, and we find that the system is unstable with frequencies and spatial structure that are in agreement with the linear theory.

2. Theoretical model

The model is sketched in figure 1 and is composed of three distinct components: the mechanics of the dam, the sloshing in the reservoir and the flow underneath the dam. We assume that the dam is a rigid structure, and the formulation of its equation of motion is relatively straightforward. For the flow dynamics, we take the fluid to be incompressible, inviscid and two-dimensional. The reservoir is also long compared to its depth ($\mathcal{H} \ll L$, where L is the length of the reservoir and \mathcal{H} is its characteristic depth), so we adopt the shallow water theory in that region. The dam, on the other hand, is inclined at an order-one angle, α , to the horizontal, so the underlying flow must develop over a horizontal length scale that is comparable to the local fluid depth, ruling out a shallow water description there. Nevertheless, the time taken for water to pass under the dam is small compared to the period of the seiches in the upstream reservoir, which also characterizes the time scale of the instability. The flow underneath the dam can therefore be treated as quasi-steady (the approximation can be made more formal by explicitly scaling the governing fluid equations with different horizontal length scales in the two distinct regions, and then taking the limit $\mathcal{H}/L \tan \alpha \ll 1$; to leading order, this removes the time derivatives from the fluid problem in the dam region). This allows us to avoid solving the full flow problem there, and instead take advantage of the ‘momentum integral method’, which expresses global conservation of mass and momentum over a control volume enclosing the dam region (see, for example, Batchelor 1967).

Note that the split between the reservoir and the dam region, marked as $x = L$ in figure 1, occurs where the shallow reservoir flow begins to be affected by the dam, or equivalently, where the flow under the dam converges upstream to one with shallow water character (this neglects any short-wavelength undulations that may be created in the reservoir by the dam; see Binder & Vanden-Broeck (2005) and the discussion in §4). Although the division is therefore naturally blurred by the flow dynamics, the dam region is relatively narrow, so the precise location is not important over distances of the order of the reservoir length. Similar arguments indicate that the downstream edge of the dam region lies where the flow separating from the dam again converges to a shallow water form.

2.1. The dynamics of the dam

The dam is constrained in such a way that it moves up and down in response to the force from the water. We describe its position by the height, h_T , of the downstream end above the base of the reservoir (see figure 1). The normal force acting on the dam is denoted F_n , of which a component $F_n \cos \alpha$ acts vertically. If the mass of the dam is m , and g is gravity, the equation of motion for the dam’s position can be written

in the form

$$I \frac{d^2 h_T}{dt^2} = F_n \cos \alpha - mg. \quad (2.1)$$

We write I , rather than m , for the inertia of the dam because, in general, the mechanism holding the dam horizontally in place may increase its inertia without contributing to the weight, as in the experiment discussed in §3.

2.2. The reservoir

The one-dimensional equations for inviscid shallow water flow in the reservoir ($0 < x < L$) are written in terms of local depth, $h(x, t)$, and flux, $q(x, t)$, as

$$\frac{\partial h}{\partial t} + \frac{\partial q}{\partial x} = 0, \quad (2.2)$$

$$\frac{\partial q}{\partial t} + \frac{\partial}{\partial x} \left(\frac{q^2}{h} \right) + gh \frac{\partial h}{\partial x} = 0, \quad (2.3)$$

with prescribed inflow

$$q = Q \quad \text{at} \quad x = 0. \quad (2.4)$$

At $x = L$, we define the flux and depth,

$$q_L(t) = q(L, t) \quad \text{and} \quad h_L(t) = h(L, t), \quad (2.5)$$

to match with the dam region.

2.3. The flow under the dam

As explained above, we treat the flow under the dam as being in steady state, on account of the length of this region being short in comparison to the reservoir. In this situation, global mass and momentum conservation across a control volume can be used to calculate the force on the dam (Batchelor 1967). The control volume (the region between the dashed lines in figure 1) extends sufficiently far upstream and downstream of the obstruction that we may match to the adjoining shallow water flow, which has its velocity independent of depth and hydrostatic pressure.

The reservoir upstream delivers fluid of depth, h_L , and speed, $u_L = q_L/h_L$. Downstream of the obstruction, the fluid layer is again shallow, with depth, h_E , and speed, u_E . Mass conservation across the control volume demands that

$$q_L = h_L u_L = h_E u_E. \quad (2.6)$$

The horizontal momentum flux in the shallow layers upstream and downstream of the dam is given by $\rho W h u^2$, where W denotes the dam's width and ρ the water density. Any change in this flux must be due to a combination of the difference in the hydrostatic pressure force, $\rho W g h^2/2$, across the volume, and the horizontal force exerted on the water by the dam, which is equal and opposite to the water force on the dam, $F_n \sin \alpha$. Thus, the vertical force in (2.1) is given by

$$F_n \cos \alpha = \frac{\rho W}{\tan \alpha} \left[h_L u_L^2 - h_E u_E^2 + \frac{1}{2} g (h_L^2 - h_E^2) \right]. \quad (2.7)$$

A third relation between q_L , h_L and h_E follows from applying Bernoulli's theorem along the bottom streamline:

$$\frac{p}{\rho} + \frac{1}{2} u^2 = g h_L + \frac{1}{2} u_L^2 = g h_E + \frac{1}{2} u_E^2, \quad (2.8)$$

so that

$$u_E = [2g(h_L - h_E) + u_L^2]^{1/2}. \quad (2.9)$$

Combining with (2.6), this implies

$$q_L^2 = \frac{2gh_L^2 h_E^2}{h_L + h_E}, \quad (2.10)$$

and using this expression in the force law (2.7) leads to

$$F_n \cos \alpha = \frac{1}{2} \frac{\rho W g (h_L - h_E)^3}{\tan \alpha (h_L + h_E)}. \quad (2.11)$$

Finally, to close the model, the downstream depth, h_E , must be related to the dam height, h_T , as

$$h_E = \mu h_T, \quad (2.12)$$

where μ is a ‘contraction ratio’ that depends upon the detailed geometry of the flow and the shape of the dam (the local radius of curvature) at the point of separation. For example, following Benjamin (1955), if the dam’s edge is relatively sharp, gravity is negligible, and the outflow is similar to potential flow through a nozzle with opening angle α ,

$$\mu(\alpha) = \left(1 + \int_0^1 \sin \alpha \theta \cot \frac{\pi \theta}{2} d\theta\right)^{-1} \quad (2.13)$$

(e.g. Batchelor 1967). This estimate takes values over the range $0.61 < \mu \leq 1$ as α decreases from $\pi/2$ to 0. In less idealized conditions, the merits of such a form for μ are ambiguous. A cruder, alternative assumption is $h_E \equiv h_T$ (i.e. $\mu = 1$), which appears to be more consistent with observations from our experiments of §3. For the present model, we adopt (2.12), taking μ to be a model parameter that depends only on the dam’s geometry.

2.4. Dimensionless model equations

In the steady state, the reservoir adjusts its depth so that the upthrust from the water flow underneath the dam balances the weight. This leads to a characteristic depth scale

$$\mathcal{H} = \sqrt{\frac{m \tan \alpha}{\rho W}}. \quad (2.14)$$

The characteristic speed for waves in the reservoir is then $\sqrt{g\mathcal{H}}$. Exploiting these scales, we introduce the dimensionless variables

$$(\check{h}, \check{h}_L) = \frac{1}{\mathcal{H}}(h, h_L), \quad \check{h}_T = \frac{\mu h_T}{\mathcal{H}}, \quad (\check{q}, \check{q}_L) = \frac{(q, q_L)}{g^{1/2} \mathcal{H}^{3/2}}, \quad \check{x} = \frac{x}{L}, \quad \check{t} = \frac{\sqrt{g\mathcal{H}}}{L} t. \quad (2.15)$$

After dropping the check decoration, the dimensionless versions of our model equations are

$$\frac{\partial h}{\partial t} + \frac{\partial q}{\partial x} = 0, \quad 0 < x < 1, \quad (2.16)$$

$$\frac{\partial q}{\partial t} + \frac{\partial}{\partial x} \left(\frac{q^2}{h} \right) + h \frac{\partial h}{\partial x} = 0, \quad 0 < x < 1, \quad (2.17)$$

$$q(0, t) = \Theta, \quad q(1, t) = q_L, \quad h(1, t) = h_L, \quad (2.18)$$

$$q_L = \frac{\sqrt{2}h_L h_T}{(h_L + h_T)^{1/2}}, \quad (2.19)$$

$$\Upsilon \frac{d^2 h_T}{dt^2} = \frac{1}{2} \frac{(h_L - h_T)^3}{h_L + h_T} - 1. \quad (2.20)$$

Two dimensionless groups appear: the non-dimensional flux through the reservoir

$$\Theta = \frac{Q}{g^{1/2} \mathcal{H}^{3/2}} = \frac{Q}{g^{1/2}} \left(\frac{\rho W}{m \tan \alpha} \right)^{3/4}, \quad (2.21)$$

and a parameter measuring the inertia of the dam

$$\Upsilon = \frac{I \tan \alpha}{\mu \rho W L^2}. \quad (2.22)$$

For the experiments reported in the next section, typical values for these two parameters are $\Upsilon \approx 0.07\text{--}0.12$ and $\Theta \approx 0.07\text{--}2.3$ (with $\mu = 1$). Note that Υ represents the ratio of natural time scales for oscillations of the dam and for waves in the reservoir, and can be varied experimentally by changing the length of the reservoir L . The second parameter, Θ , can be varied by changing the effective mass of the dam m (a larger weight on the dam corresponds to smaller Θ).

The formulation above assumes that the dam never touches the bottom of the reservoir; if such a collision occurs, the resulting impulse must be added to (2.20) to ensure that h_T remains positive.

2.5. Steady states and their linear stability

The steady solution to the system (2.16)–(2.20) has $q = q_L = \Theta$ and $h = h_L$ (to satisfy (2.16) and (2.17)), with the depths $h_L = H_L$ and $h_T = H_T$ given by solving the algebraic problem:

$$\Theta^2 = \frac{2H_L^2 H_T^2}{H_L + H_T}, \quad 2 = \frac{(H_L - H_T)^3}{H_L + H_T}. \quad (2.23)$$

The solutions, $H_T(\Theta)$ and $H_L(\Theta)$, are illustrated in figure 2. Corresponding dimensional steady states are shown later in figure 11, for varying weight on the dam.

We explore the stability of this state by introducing small normal-mode perturbations about the equilibrium,

$$q = \Theta + \sigma(x)e^{-i\omega t}, \quad h = H_L + \eta(x)e^{-i\omega t}, \quad h_T = H_T + \eta_T e^{-i\omega t}, \quad (2.24)$$

where ω is the (complex) frequency. After linearizing in the amplitudes, σ , η and η_T , we arrive at the system

$$\frac{\partial \sigma}{\partial x} - i\omega \eta = 0, \quad \frac{2\Theta}{H_L} \frac{\partial \sigma}{\partial x} - i\omega \sigma + H_L \left(1 - \frac{\Theta^2}{H_L^3} \right) \frac{\partial \eta}{\partial x} = 0, \quad (2.25)$$

$$\sigma(0) = 0, \quad \sigma(1) = \sigma_L, \quad \eta(1) = \eta_L, \quad (2.26)$$

$$\sigma_L = \Theta \frac{(H_L + 2H_T)}{2H_L(H_L + H_T)} \eta_L + \Theta \frac{(2H_L + H_T)}{2H_T(H_L + H_T)} \eta_T, \quad (2.27)$$

$$\left(\frac{H_L + 2H_T}{H_L^2 - H_T^2} \right) \eta_L - \left(\frac{2H_L + H_T}{H_L^2 - H_T^2} - \frac{1}{2} \Upsilon \omega^2 \right) \eta_T = 0. \quad (2.28)$$

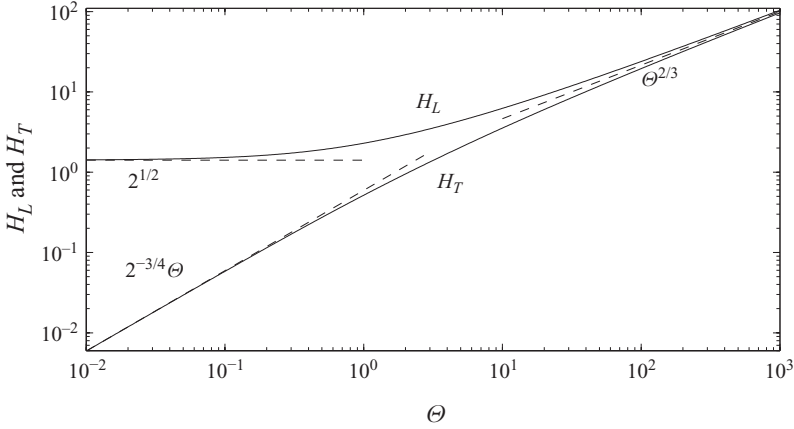


FIGURE 2. Equilibrium depths, H_T and H_L , against Θ , as given by (2.23). For $\Theta \rightarrow 0$, $H_T \rightarrow 2^{-3/4}\Theta$ and $H_L \rightarrow 2^{1/2}$; for $\Theta \gg 1$, $H_T \sim \Theta^{2/3}$ and $H_L \sim \Theta^{2/3}$.

The solution to (2.25) and (2.26) for the reservoir seiche is

$$\sigma = 2ie^{-iF\omega x/\omega_0} \sin \frac{\omega x}{\omega_0}, \quad \eta = \frac{2}{\omega_0} e^{-iF\omega x/\omega_0} \left(\cos \frac{\omega x}{\omega_0} - iF \sin \frac{\omega x}{\omega_0} \right), \quad (2.29)$$

where

$$F = \frac{\Theta}{H_L^{3/2}}, \quad \omega_0 = H_L^{1/2}(1 - F^2). \quad (2.30)$$

(Note that F is the Froude number of the mean flow through the reservoir.) Thus,

$$\eta_L = -\frac{1}{\omega_0} \left(i \cot \frac{\omega}{\omega_0} + F \right) \sigma_L, \quad (2.31)$$

and after a little algebra with (2.27) and (2.28) we arrive at the dispersion relation

$$D(\omega) = a_2 + a_1 a_3 - \Upsilon a_1 \omega^2 - i[(a_3 - \Upsilon \omega^2)(\omega_0 + a_1 F) + a_2 F] \tan \frac{\omega}{\omega_0} = 0, \quad (2.32)$$

where

$$a_1 = \frac{\Theta(H_L + 2H_T)}{2H_L(H_L + H_T)}, \quad a_2 = \frac{\Theta(2H_L + H_T)(H_L + 2H_T)}{H_T(H_L + H_T)(H_L^2 - H_T^2)}, \quad a_3 = \frac{2(2H_L + H_T)}{H_L^2 - H_T^2}. \quad (2.33)$$

Solutions of the dispersion relation are illustrated in figures 3 and 4; the spectra are symmetrical under reflection about the imaginary axis; the modes are either real, with purely imaginary frequency, or come out as complex pairs, with $\omega = \pm |\omega_r| + i\omega_i$. We therefore focus on those in the right-half plane ($\omega_r \geq 0$). The first figure tracks the eigenvalues for varying Θ at fixed Υ ; the second figure shows how the eigenvalues vary with Υ at fixed Θ . The spectrum contains one real mode that is always damped (labelled as ‘mode 0’ in the figures). The other modes are all complex, a subset of which, depending on the parameter values, can be unstable ($\omega_i > 0$). In other words, the model predicts the exponential growth of oscillatory modes.

The complex modes can be split into two varieties in certain limits of Θ and Υ : when $\Theta \gg 1$, all but one of the complex modes converge to the same growth rate and have regularly spaced frequencies given by $n\pi\omega_0$, with n an integer (see figure 3, where they are labelled by n). Similarly, in the limit of either $\Upsilon \ll 1$ or $\Upsilon \gg 1$, the modes

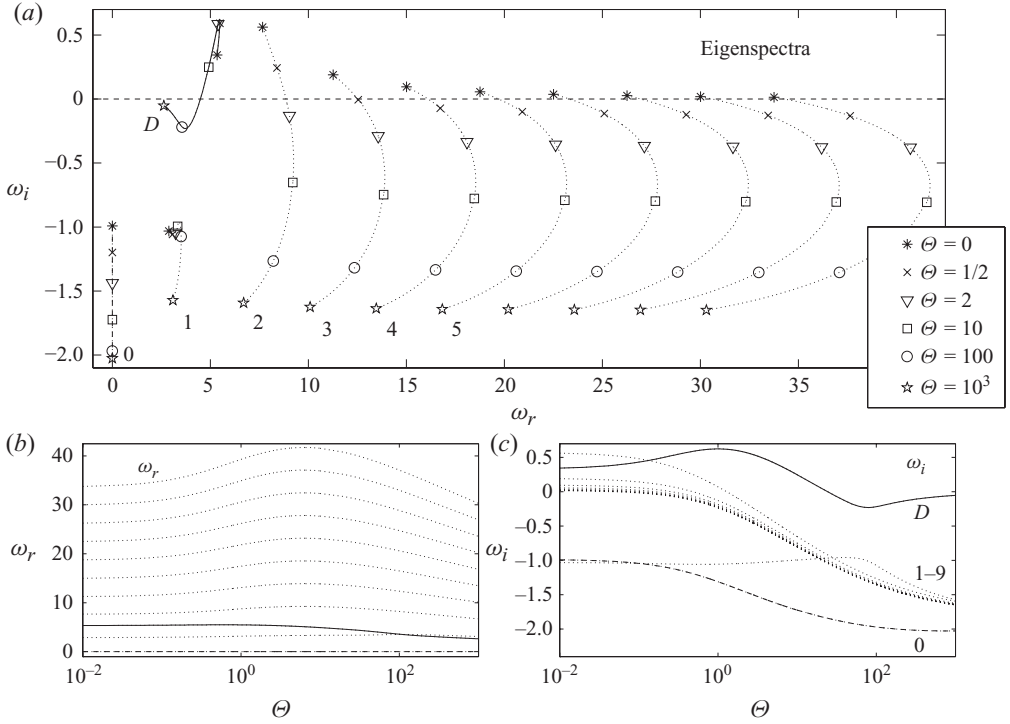


FIGURE 3. Real and imaginary parts of the 11 lowest frequency roots of dispersion relation (2.32) for $\Upsilon = 0.12$ and varying Θ . Panel (a) shows the eigenvalues on the spectral plane, with the lines showing the variation with Θ , and eigenvalues for particular choices of Θ plotted as various types of points (as indicated in the legend). The labels refer to the classification scheme outlined in the main text; the dotted lines show the ‘seiche modes’, the solid line is the ‘dam mode’ and the dashed line shows the purely real mode. Panels (b) and (c) show the frequency and growth rates against Θ .

again converge to such a sequence. These modes are related to the normal modes of a reservoir with a fixed dam (accessible in the current dimensionless notation by taking the limit $\Upsilon \rightarrow \infty$, which makes the dam infinitely massive); i.e. they are the ‘seiche modes’.

The complex mode that stands out from this infinite set can be identified as a mode associated with the dam itself: a linearization of the dam’s equation of motion (2.20) provides a simple harmonic oscillator equation for the perturbation in dam height, $h_T - H_T$, driven by fluctuations in upstream water depth, and with a natural frequency of $\sqrt{a_3/\Upsilon}$. The coupling with the reservoir modifies the frequency of this ‘dam mode’, but it can be recognized in the spectrum by its distinctive behaviour for large Θ (where its growth rate vanishes, see figure 3c), and its dependence on $\Upsilon^{-1/2}$ in the limit $\Upsilon \gg 1$ (see figure 4a).

Although the complex modes are distinguishable in various limits of the two parameters, Θ and Υ , this does not remain the case for intermediate parameter settings: as illustrated in figure 4, there is a complicated interaction between the modes involving a sequence of avoided crossings occurring close to when the base frequencies of the seiche modes intersect the natural dam frequency (a similar feature characterizes the simple model of a clarinet explored by Wilson & Beavers 1974). The close relation of this interaction with the instability mechanism is highlighted

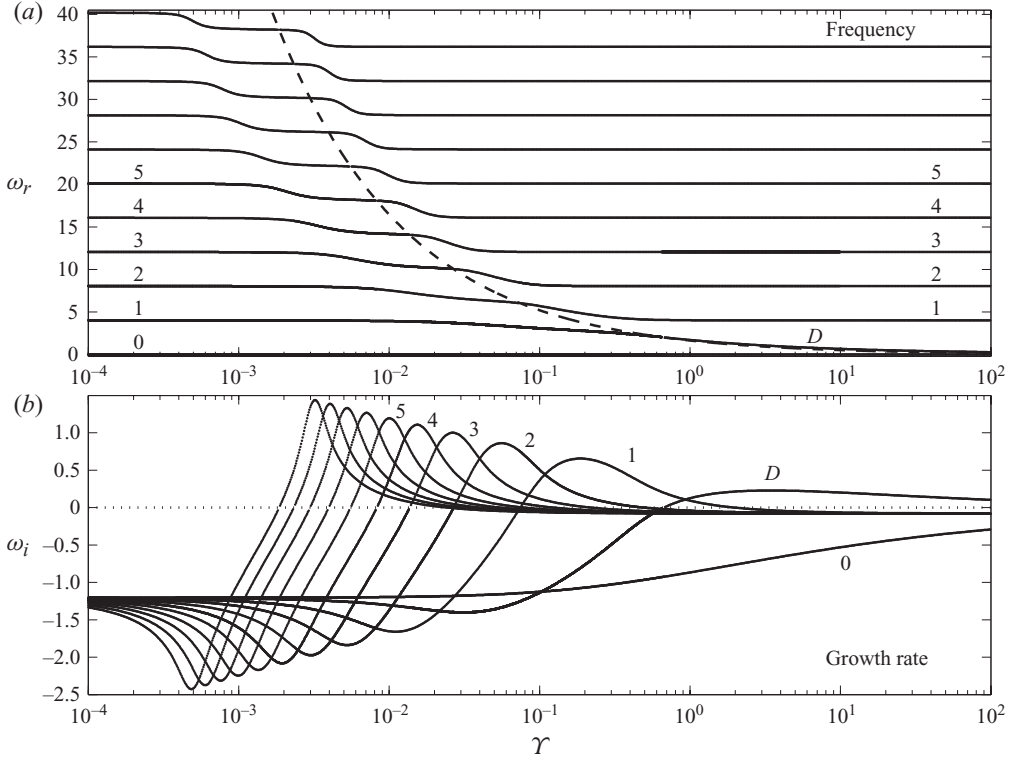


FIGURE 4. Variation of (a) frequency and (b) growth rate with γ for $\Theta = 1/4$. The 11 lowest frequency modes are shown. In (a), the dashed line shows the frequency, $\gamma^{-1/2} \sqrt{a_3}$. The labels refer to the classification scheme outlined in the main text.

by the growth rates, which peak near those intersections. Consequently, the most unstable mode at a particular parameter setting is difficult to identify as either a seiche mode or a dam mode. Instead, it has a character that is a mix of both.

Note that the modes in figure 3 all become stable if Θ is taken sufficiently large. In other words, instability should disappear at sufficiently high flow rate or for very low dam weight, at least for this particular value of γ . In fact, the picture is more complicated for other values of this parameter, as shown in the next subsection. Also, the most unstable modes for fixed Θ (in figure 4) occur at the smallest values of γ and with relatively high frequencies (the maximal low- γ growth rates are $O(\log \gamma^{-1})$ and their frequencies are $O(\gamma^{-1/2})$). However, the model ignores the viscous damping of the seiche, which occurs in Stokes layers adjacent to the sides and bottom of the reservoir and becomes prominent at high frequency (Keulegan 1959).

The spatial structure of the unstable modes is illustrated in figure 5. These two particular examples correspond to instabilities with similar spatial structure to the gravest two seiche modes. Note that the modes are not pure standing waves: as is evident from the form of the solution in (2.29), the modes have the character of both a standing and a progressive wave (the real part of $\sigma e^{-i\omega t}$, for example, is $2 \sin(\omega x / \omega_0) \sin(\omega(t + Fx / \omega_0))$).

2.6. Stability boundaries

To locate the regions of parameter space in which the system is unstable, we look for solutions with purely real frequency to the dispersion relation, $D(\omega) = 0$; these

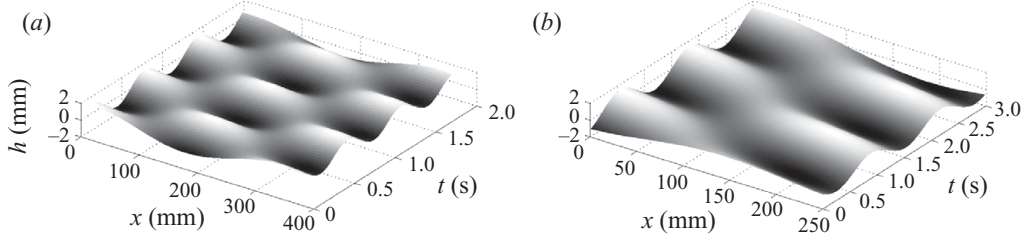


FIGURE 5. The most unstable linear modes in the reservoir for (a) $\Theta = 0.18$ and $\Gamma = 0.07$ (corresponding to the experiment shown later in figure 9) and (b) $\Theta = 1.39$ and $\Gamma = 0.12$ (corresponding to the experiment shown later in figure 10). The amplitude here is arbitrary, but has been chosen to correspond to those observed in the experiments.

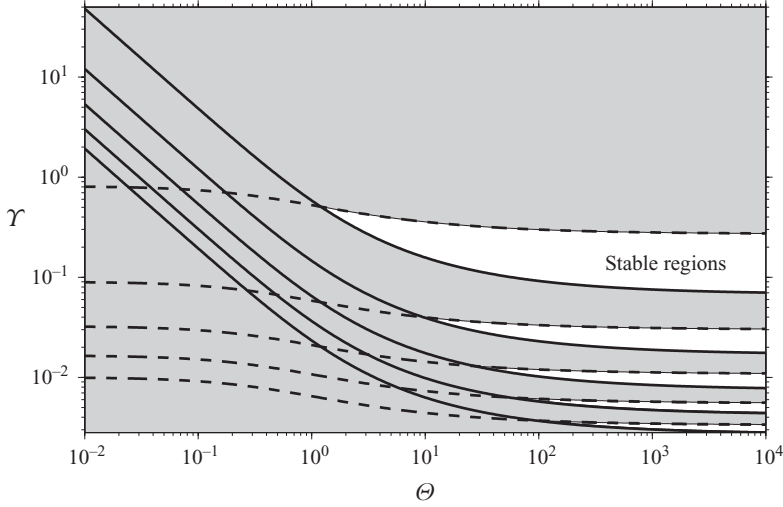


FIGURE 6. Modal stability boundaries on the (Θ, Γ) -plane. The solid lines show $\Gamma = f_1(\Theta)/j^2$ and the dashed lines show $\Gamma = f_2(\Theta)/(2j-1)^2$ for $j = 1-5$. The shaded areas are unstable.

special modes trace out stability boundaries on the (Θ, Γ) -plane. The (positive) real frequencies come in two varieties: either

$$a_2 + a_1 a_3 = \Gamma a_1 \omega^2 \quad \text{and} \quad \sin(\omega/\omega_0) = 0, \quad (2.34)$$

or

$$a_3 + \frac{F a_2}{\omega_0 + F a_1} = \Gamma \omega^2 \quad \text{and} \quad \cos(\omega/\omega_0) = 0. \quad (2.35)$$

Hence,

$$\Gamma = \frac{f_1(\Theta)}{j^2} \equiv \frac{a_2 + a_1 a_3}{a_1 j^2 \pi^2 \omega_0^2} \quad \text{or} \quad \Gamma = \frac{f_2(\Theta)}{(2j-1)^2} \equiv \frac{4[a_3(\omega_0 + F a_1) + F a_2]}{(2j-1)^2 \pi^2 \omega_0^2 (\omega_0 + F a_1)}, \quad (2.36)$$

where j is a positive integer. The boundaries in (2.36) are illustrated for $j = 1-5$ in figure 6.

With a little more algebra, one may show that a mode becomes unstable *below* the first of these boundaries (shown by solid lines in figure 6). Conversely, a mode becomes unstable *above* the second of the boundaries (the dashed lines in the figure). Referring

back to figure 4, we also see that, on increasing Υ at fixed Θ , particular modes become unstable at $\Upsilon = f_2(\Theta)/(2j+1)^2$, and then return to stability at $\Upsilon = f_1(\Theta)/j^2$ for the same integer j . Thus, pairs of the stability boundaries map out ‘tongues’ on the parameter plane within which a particular mode is unstable. Altogether, we can then identify the unstable regions of the parameter plane, which are shown shaded in figure 6. The section at $\Upsilon = 0.12$ in figure 3 fortuitously cuts through one of the slender windows of stability that extend to large Θ when Υ is sufficiently small.

Note that the system is always unstable for $\Theta < 1.15$, and the entire region of large Υ is unstable due to a single mode. This is the dam mode whose frequency and growth rate for $\Upsilon \gg 1$ can be shown to be

$$\omega \sim \Upsilon^{-1/2} \sqrt{\frac{a_2 + a_1 a_3}{a_1}} + i \Upsilon^{-1} \frac{a_2}{2a_1^2}. \quad (2.37)$$

2.7. The low through-flow limit, $\Theta \ll 1$

The equilibrium equations and dispersion relation reduce to a simpler form in the limit $\Theta \ll 1$, which is relevant for many of the experiments in the next section. In this limit, the steady state is

$$q = \Theta, \quad H_L = 2^{1/2}, \quad H_T = \frac{\Theta}{2^{3/4}} \quad (2.38)$$

and the dispersion relation (2.32) reduces to

$$D(\omega) = 2^{1/4} [2 + i(\Upsilon \omega^2 - 8^{1/2}) \tan(2^{-1/4} \omega)] = 0. \quad (2.39)$$

The solutions with large frequency, $\omega_r \sim 2^{1/4} n\pi$, for integral $n \gg 1$, have growth rate

$$\omega_i \sim 2^{1/4} \tanh^{-1} \left(\frac{2^{1/2}}{n^2 \pi^2 \Upsilon - 2} \right), \quad (2.40)$$

and can be identified as the seiches modes of the reservoir; provided n is sufficiently large, the flow destabilizes these normal modes.

The low- Θ limit also leads to an interesting illustration of the feedback mechanism underlying the unstable seiches. The size of depth perturbations to the reservoir is of order Θ , and after introducing $h - H_L = \Theta \zeta$ and $h_T - H_T = \Theta \zeta_T$, the model reduces to a wave equation in the reservoir,

$$\frac{\partial^2 \zeta}{\partial t^2} = c^2 \frac{\partial^2 \zeta}{\partial x^2}, \quad \left[\frac{\partial \zeta}{\partial x} \right]_{x=0} = 0, \quad (2.41)$$

coupled to an oscillator at the dam,

$$\Upsilon \frac{d^2 \zeta_T}{dt^2} = c^2 [\zeta(1, t) - 2\zeta_T], \quad \left[\frac{\partial \zeta}{\partial x} \right]_{x=1} = -c \dot{\zeta}_T, \quad (2.42)$$

where $c = 2^{1/4}$ is the wavespeed.

In view of the boundary condition at $x = 0$ and because we are primarily interested in the solution at the downstream end, $x = 1$, we solve the wave equation in terms of d’Alembert’s solution,

$$\zeta = F(t + x/c - 1/c) + F(t - x/c - 1/c), \quad (2.43)$$

where the unknown function, $F(t)$, is determined by the flux condition in (2.42):

$$F(t) = F(t - T) - c^2 \zeta_T(t), \quad (2.44)$$

with $T = 2/c$. The physical interpretation of this result is that the disturbance in the reservoir can be broken down into the sum of incoming and outgoing waves; the latter is perfectly reflected at the upstream end of the reservoir and subsequently returns to the dam after the temporal delay, T . The relation in (2.44) is the subsequent downstream reflection condition; the returning wave is partly transmitted under the dam according to the motion of that obstruction, but also launches a new wave back into the reservoir.

The finite propagation time for waves in the reservoir thereby generates a delay term in (2.42):

$$\frac{d^2 \zeta_T}{dt^2} + \frac{2c^2}{\gamma} \zeta_T = \frac{c^2}{\gamma} [F(t) + F(t - T)]. \quad (2.45)$$

From (2.45), we may formulate an energy equation,

$$\frac{d}{dt} \left(\frac{1}{2} \dot{\zeta}_T^2 + \frac{c^2}{\gamma} \zeta_T^2 \right) = \frac{c^2}{\gamma} [F(t) + F(t - T)] \dot{\zeta}_T \equiv \frac{c^2}{\gamma} \zeta_L \dot{\zeta}_T. \quad (2.46)$$

Thus, when the phase of $\dot{\zeta}_T$ can be suitably tuned with respect to the upstream pressure variation, ζ_L , energy can be fed into the oscillator.

Note that a similar (but slightly more complicated) energy argument can be made for linearized perturbations with arbitrary Θ : the linearized version of (2.20) again can be reduced to a delayed oscillator equation with an energy source proportional to $(h_L - H_L)dh_T/dt$, so that unstable oscillations can be generated by perturbations in water depth that have a suitable phase with respect to the dam motion. Nevertheless, no linearization has been applied to arrive at (2.45) and (2.46) the nonlinear terms appearing in the original model system are all order Θ or smaller. This suggests that the main limitation to the amplitudes of the unstable seiches modes in this limit arises because the dam eventually strikes the bottom.

3. Experiments

3.1. Experimental set-up

The set-up for our experiments is illustrated in figure 7: a pump circulates water through a feeder tank that delivers a constant flux Q into the adjoining main reservoir. The dam is an inclined plate that is almost as wide as the tank; millimetre gaps to either side are required to allow the dam to move freely, but inevitably allow a small amount of fluid to leak around the sides. The damming plate is attached to a horizontal arm that is pivoted downstream of the reservoir, allowing the obstruction to move up and down. Since it is attached to the pivot and must therefore move in an arc, there is also a small amount of sideways motion of the dam, in contrast to the purely vertical motion of the model. The sideways motion, of order 1 mm compared to the reservoir length of around 30 cm, has very little effect on the dynamics.

Provided the rotation of the pivoted arm is not too large, the vertical position of the dam can adequately be described by the theoretical model in (2.1). To see this, we use an angle $\theta(t)$ to orientate the arm, as shown in figure 7; the equation of motion for the structure can be written as

$$\mathcal{J} \frac{d^2 \theta}{dt^2} = a F_n \cos(\alpha + \beta) - M, \quad (3.1)$$

in which \mathcal{J} is the moment of inertia of the whole arm arrangement, M is the gravitational moment applied to weigh down the dam (discussed below) and F_n is the

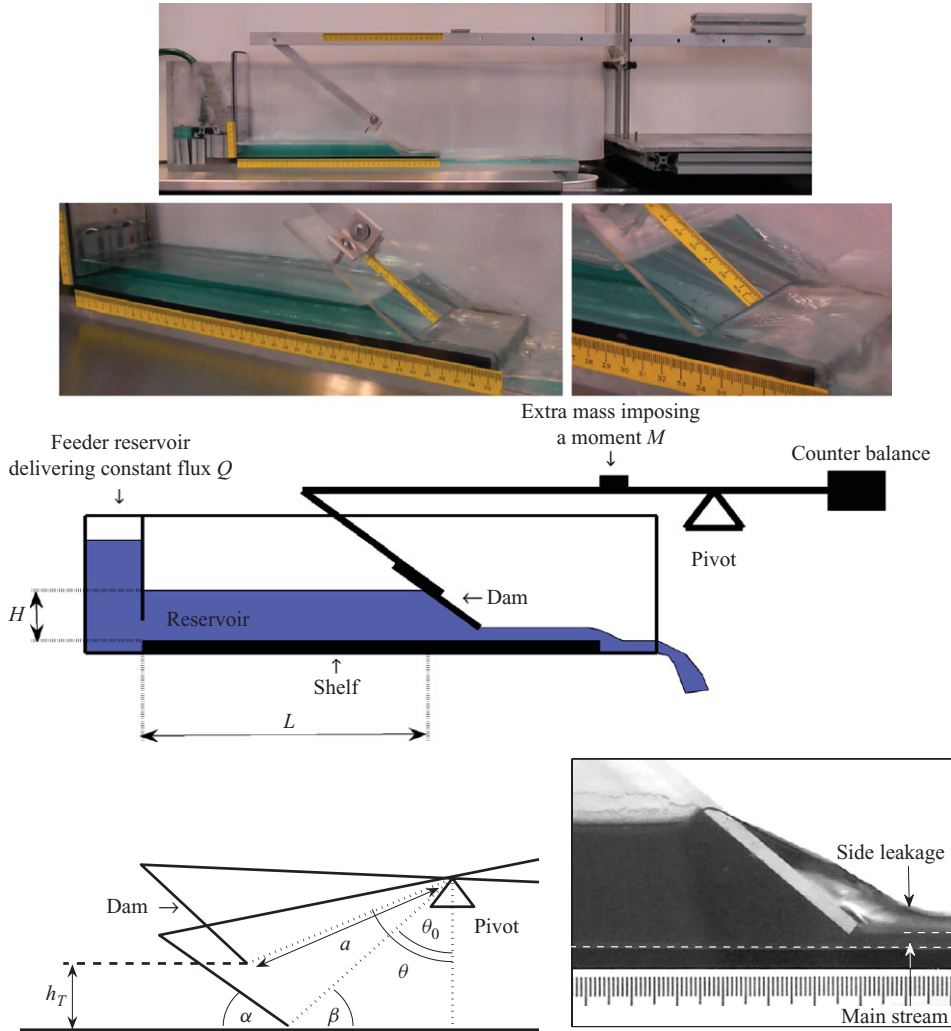


FIGURE 7. (Colour online available at journals.cambridge.org/FLM) Photographs of the experiment, showing the circulation of water through a reservoir in a rectangular tank, of width 10 cm, length 70 cm and height 30 cm. The reservoir is dammed by an inclined Plexiglas plate attached to an arm that rotates freely about a pivot. The two pictures in the bottom row show the geometry of the arm and a photograph from the side of the flow under and around the dam. The water is dyed with ink, so the main bulk of the stream is apparent as the darker fluid layer; the dashed lines highlight the bottom and the surface of the stream.

normal force generated by the water flow. The other constants in (3.1) describe the geometry: a is the distance to the pivot from the point where the dam touches the bottom of the tank, β is the angle between this line and the horizontal and α is the angle of the dam. Note that the lift force F_n is taken to act at the bottom of the dam in (3.1), whereas in reality it is distributed over the wetted length of that obstacle; since the wetted length is much less than a , this approximation is not significant.

The variations in θ in the experiment are small ($\leq 1^\circ$), so it is appropriate to convert this equation into the form of (2.1) by noting that

$$h_T(t) = a \cos \theta - a \cos \theta_0 = a(\theta - \theta_0) \cos \beta + O((\theta - \theta_0)^2), \quad (3.2)$$

where $\theta_0 = \pi/2 - \beta$ is the resting value of θ on the bottom (cf. figure 7). In terms of h_T , the equation of motion is therefore

$$\frac{\mathcal{I} \cos \alpha}{a^2 \cos \beta \cos(\alpha + \beta)} \frac{d^2 h_T}{dt^2} = F_n \cos \alpha - \frac{M \cos \alpha}{a \cos(\alpha + \beta)}, \quad (3.3)$$

which is equivalent to (2.1) with the dam's weight mg given by $M \cos \alpha / a \cos(\alpha + \beta)$, and inertia I given by $\mathcal{I} \cos \alpha / a^2 \cos \beta \cos(\alpha + \beta)$.

To control the moment during the experiments, the dam was counterbalanced with a weight on the opposite side of the pivot, and then additional masses were added to the arm to generate a net downward moment on the dam side of the pivot. This applied moment in principle depends upon the rotation of the arrangement about the pivot, since the component of gravity that acts as a moment varies with the location of the centre of mass. Because the variations in angle incurred in our experiments are very small, the moment can largely be treated as constant, as in the theoretical model. We therefore define M to be the moment as measured when the dam rests on the bottom of the reservoir, and use this value to compare the theoretical and experimental results. However, there is an error that cannot be completely ignored at the smallest applied moments, and this is discussed further in Appendix A. Ignoring this error, and because the main body of the arm remains roughly horizontal, we write the moment M as

$$M = M_0 + m_a g \Delta, \quad (3.4)$$

where M_0 is the moment of the arm and dam alone (determined by adding or subtracting masses until it is counterbalanced), and m_a denotes the additional mass placed on the arm at a distance Δ from the pivot.

The typical values for the experimental parameters were $\mathcal{I} \approx 0.13 \pm 0.01 \text{ kg m}^2$, $\alpha \approx 38 \pm 1^\circ$, $\beta \approx 25 \pm 1^\circ$, $a \approx 48 \pm 0.2 \text{ cm}$, $g \approx 10 \text{ m s}^{-2}$, $\rho \approx 1000 \text{ kg m}^{-3}$, $W \approx 10 \pm 0.2 \text{ cm}$, $Q \approx 1.2 \pm 0.05 \times 10^{-3} \text{ m}^2 \text{ s}^{-1}$, and the main parameters that were varied were the reservoir length $L \approx 27\text{--}36 \text{ cm}$ and the moment $M \approx 0\text{--}0.3 \text{ Nm}$. For a comparison with the model in the previous section, we take the flow depth downstream of the dam (h_E) to be equal to its height, h_T (i.e. $\mu = 1$), guided by observations such as that shown in figure 7 (which was typical of all our experiments). We then estimate

$$\Upsilon \approx 0.07 - 0.12 \quad \text{and} \quad \Theta \approx 0.07 - 2.3 \quad (3.5)$$

(the largest value of Θ corresponds to the smallest recorded moments, but the vast majority of measurements have $\Theta < 1$). Furthermore, given reservoir depths of a few centimetres, the Reynolds number, $Re = Q/\nu \sim 10^3$, and the Bond number, $Bo = \rho g \mathcal{H}^2 / \sigma_w \sim 10^2$, where $\nu \approx 10^6 \text{ m}^2 \text{ s}^{-1}$ is the kinematic viscosity and $\sigma_w \approx 7 \times 10^{-2} \text{ N m}^{-1}$ is the surface tension of water in air. Thus, viscous and capillary effects likely play a relatively minor role, in line with the assumptions of our theoretical model. Note that in all the experiments, the downstream flow appeared to be too fast to support any wave-like features of the kind found behind sluice gates (e.g. Benjamin 1955).

3.2. Phenomenology

As predicted theoretically, the flow state established once the pump began to circulate water through the reservoir became unsteady due to the coupling of seiches in the reservoir with flow underneath the dam. The dam oscillations initially grew in amplitude but then saturated to furnish a roughly periodic state. From video recordings of the reservoir and dam, we were able to extract measurements of water depths and dam heights. Sample time series of dam height (h_T) are displayed in

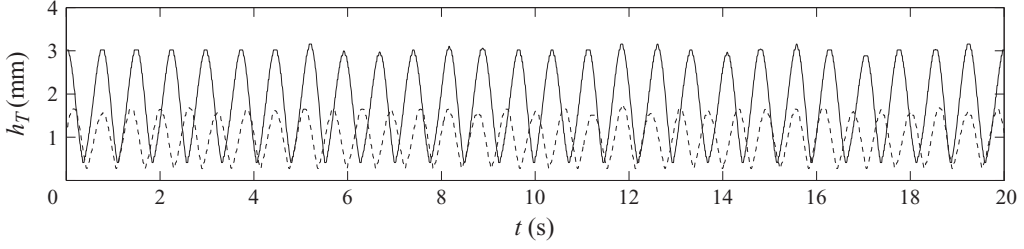


FIGURE 8. Example time series of dam height, h_T , with reservoir length, $L = 27$ cm, flux $Q = 1.2 \times 10^{-3} \text{ m}^2 \text{ s}^{-1}$ and moment of inertia $\mathcal{I} = 0.13 \text{ kg m}^2$. The solid line is for an imposed moment of 0.08 N m , whereas the dashed line shows the same experiment with increased moment of 0.16 N m .

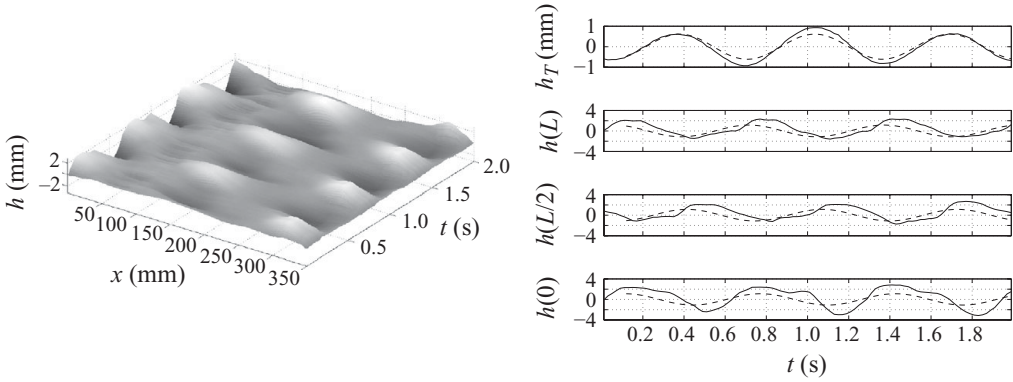


FIGURE 9. (a) Water surface in the reservoir as determined from video footage. The applied moment is $M = 0.09 \text{ N m}$, and the reservoir length is $L = 36$ cm. (b) Dam height, h_T , and reservoir depths near the dam, near the middle and at the upstream end. The dashed lines show the prediction of the linear theory for the most unstable mode with amplitude chosen to match the first oscillation of h_T .

figure 8. Oscillations are relatively regular but fairly nonlinear: the peak-to-trough amplitude is of the order of the mean, with the dam coming close to the bottom but not striking it (in other situations, there was a recognizable impact of the gate with the bottom, but more often than not, the outflow remained open). Perturbation amplitudes are rather less significant in the reservoir, with the seiches causing depth variations of 10% or less.

Detailed measurements of water depth in the reservoir from one experiment are shown in figure 9. Figure 9a shows the water depth, $h(x, t)$, as a surface above the (x, t) -plane, and clearly reveals how the sloshing has the character of the second seiche mode of the reservoir. The time series in figure 9b illustrates this further, with the depths at the two ends of the reservoir oscillating largely in phase whilst the depth at the halfway point is out of phase. Note that the dam height noticeably lags behind the adjacent free surface displacement, h_L , which is more closely tuned to h_T (cf. (2.46)).

A second example of the free surface displacement from an experiment with a different moment and reservoir length is shown in figure 10. In this case, the modal structure is more like the gravest seiche mode, with the two ends oscillating out of phase and the depth halfway down the reservoir being close to a node. The two

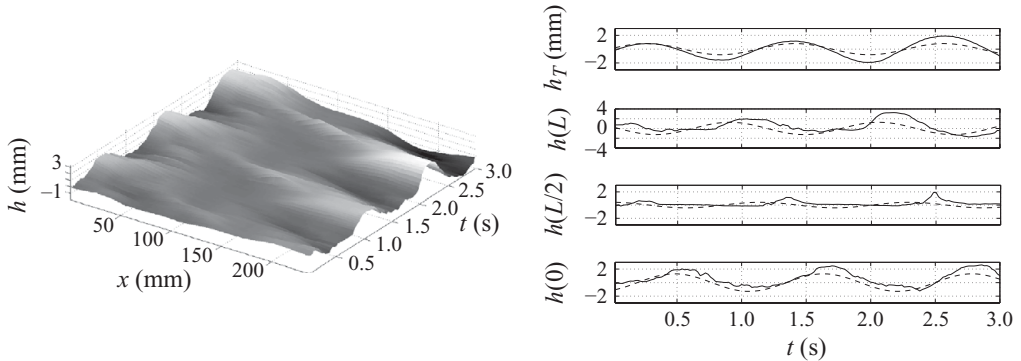


FIGURE 10. (a) Water surface in the reservoir as determined from video footage, with applied moment $M = 0.006 \text{ N m}$ for a reservoir length of $L = 27 \text{ cm}$. (b) Dam height, h_T , and reservoir depths near the dam, near the middle and at the upstream end. The dashed lines show the prediction of the linear theory for the most unstable mode with amplitude chosen to match the first oscillation of h_T .

experiments in figures 9 and 10 correspond to the theoretical examples shown earlier in figure 5; the overall structure of the modes is reproduced by the model.

3.3. Steady states

We varied parameters in the experiments more systematically by adjusting the applied moment, M , for a small number of different reservoir lengths, L , fixing the flow rate, Q , and the dam's angle, α , and inertia, \mathcal{I} .

We first recorded measurements of the steady equilibrium states. Because these states are typically unstable, it is not possible to directly observe them without modifying the experimental set-up. To this end, we added an additional dissipation by suspending from the arm a weight immersed in a relatively viscous fluid (golden syrup); the extra friction provided by this dashpot dominated the destabilization of the seiche. The steady state depths, h_L and h_T , measured accordingly are shown in figure 11(a), where they are compared with theoretical predictions. Measurements of water depth h were accurate to $\pm 2 \text{ mm}$, and for the dam height, to $\pm 0.25 \text{ mm}$. Most of these moments correspond to $\Theta < 1$ in figure 2, and the dimensional depths are therefore predicted to scale as $h_L \sim M^{1/2}$ and $h_T \sim M^{-1/4}$.

The observed outflow depth, h_T , is typically less than the model predictions. We believe this discrepancy is mostly due to two effects. First, although the gaps on either side of the dam are small (about 1.5 mm), h_T also becomes small for the larger moments. In these situations, a significant fraction of the flow that would otherwise have to pass underneath the dam is actually diverted around the sides. To quantify the effect, we repeated the experiments with a wider experimental tank and dam; the gaps, being of comparable size, were proportionately smaller. Figure 11(b) shows the results; the measured depths are indeed much closer to the two-dimensional theory.

Second, a further discrepancy between the experiments and theory occurs at small M due to the slight variation in moment with dam position. This effect can be quantified by observing the height at which the dam is perfectly balanced when a small counterbalancing moment is applied without any water flow; that information can then be used to recalculate the true moment acting when the dam is lifted by water pressure to a given equilibrium position. Appendix A provides technical details.

Leakage around the sides can also be incorporated into the theoretical model, as described in Appendix B. Once we incorporate both the variation of the moment and

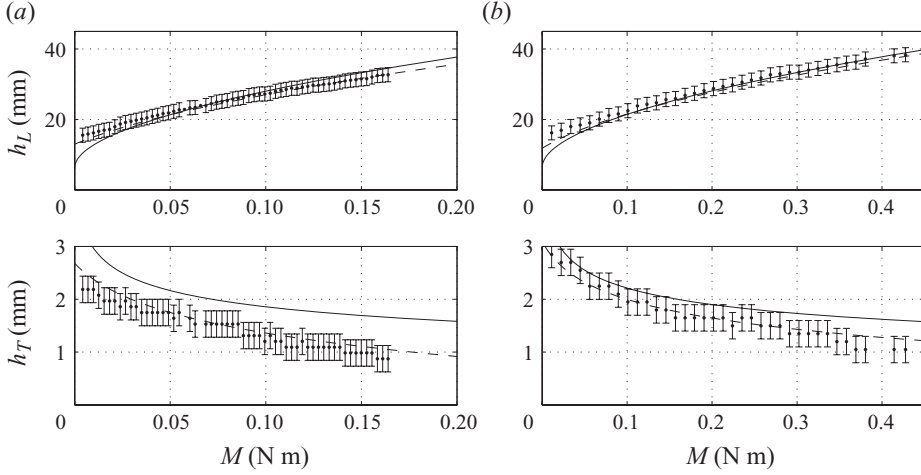


FIGURE 11. (a) Steady state depths h_T and h_L measured experimentally with a dashpot used to stabilize the arm (dots) along with model predictions from §2.5 (solid line). The dashed line shows the results of an improved theory accounting for the flow through the gaps at the sides of the paddle and the variation of the moment with angle, as described in Appendix A and Appendix B. (b) The equivalent measurements and theory for a wider reservoir, when flow around the sides of the dam has relatively less effect.

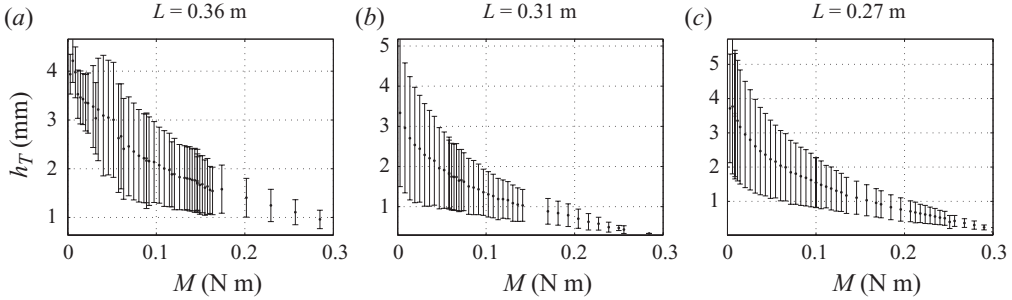


FIGURE 12. (a)–(c) Dots show the mean dam height as the moment is varied for three different reservoir lengths. Error bars showing the standard deviation from this mean during the oscillations, giving a measure of the amplitude of oscillations.

the side leakage into the theory, most of the discrepancies between the model and the theory are removed. This is illustrated in figure 11, where the ‘improved model’ of Appendices A and B is also compared with the experiments.

3.4. Unstable modes

We now display results for the system without the dashpot. Time series of dam depth (h_T), such as that in figure 8, were analysed to determine the mean position, and the amplitude and period of the variations about that level were then recorded. Figure 12 shows the mean values of h_T for varying moment, for three different reservoir lengths. The error bars display the standard deviation from that mean arising due to the oscillations of the dam, and therefore provide a measure of the amplitude of the instability. Because the dam oscillations are not perfectly sinusoidal, and multiple frequencies are clearly present in the signal (examples of less regular oscillations are presented below), a determination of oscillation period is more delicate. We define a ‘dominant frequency’ by taking a Fourier transform of the time series of h_T and

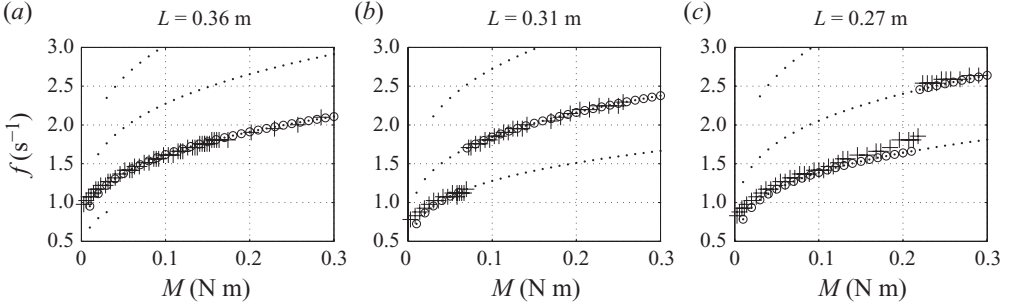


FIGURE 13. Comparison of frequencies found in experiment and linear theory. Dots show the dimensional cyclic frequencies of unstable modes according to the theory, (2.32), $\omega_r \sqrt{g\mathcal{H}}/2\pi L$, and the circles show the unstable mode with the largest growth rate. Crosses show the dominant frequency in the experiment as determined from the peak in the spectrum of the time series of h_T .

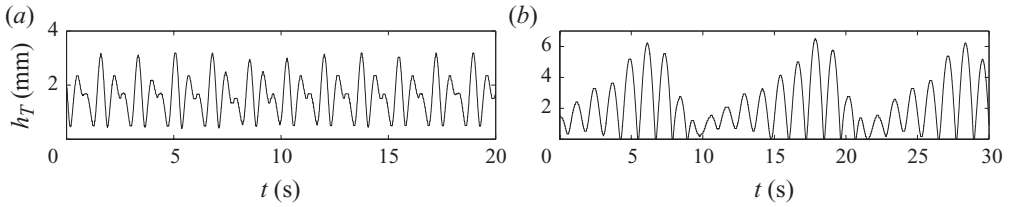


FIGURE 14. (a) An example of the beating motion of the dam during the transition between two dominant frequencies, with $M = 0.075$ N m, and $\mathcal{J} = 0.13$ kg m². (b) Time series from an experiment with moment 0.003 N m, and much larger moment of inertia, $\mathcal{J} = 0.27$ kg m². In both cases, the reservoir length was $L = 31$ cm and the flux was $Q = 1.2 \times 10^{-3}$ m² s⁻¹.

recording the frequency of the peak with most power. Figure 13 shows how this dominant frequency varies with the moment, and compares it with the frequency of the most unstable mode predicted theoretically (typically, there are multiple unstable modes at the parameter settings corresponding to the experiments). The overall agreement between the two is remarkable.

The observed oscillation spectra typically exhibit multiple peaks, and the dominant frequency displays sudden jumps where one peak overtakes another. The change in height of the individual peaks in the Fourier spectra is, however, more gradual as the moment is varied. Simultaneously, there is a gradual change in the spatial structure of the reservoir mode, ranging from a shape like that of the second seiche mode (figure 9) at the higher moments to one more like the gravest mode (figure 10).

Because our theory is confined to linear stability analysis, we are unable to account for this smooth transition in the modal properties, nor for the systematic amplitude variation seen in figure 12. The observed situation seems more analogous to a problem of constructive nonlinear mode competition. Indeed, during the frequency transitions, the motion of the dam is visibly more complex; an example time series from such a situation is shown in figure 14(a). This type of beating pattern was fairly typical for the moments close to the transitions, and reflects the intrinsic nonlinear mode coupling.

Another type of nonlinearity is illustrated in figure 14(b), which shows the time series for an experiment with different physical parameters than used for the main part of our study. More mass was added to the pivot system to increase the moment of

inertia (to $\mathcal{I} = 0.27 \text{ kg m}^2$, instead of $\mathcal{I} = 0.13 \text{ kg m}^2$). In this experiment, the growth rate of the instability is relatively small, but the oscillations continue to gain amplitude until the dam abruptly hits the bottom in a small number of impacts. The instability is thereby knocked out of its rhythm, and the fluctuations in the reservoir and dam then decay until the instability is once more able to grow from low amplitude.

4. Discussion

Our goal in the present work has been to provide a theoretical and experimental study of a novel instability of a simple hydrodynamic system. This system consists of a reservoir held by a movable dam in which through-flow unstably couples reservoir seiches with dam oscillations. Our theoretical model of the configuration couples shallow water seiches in the reservoir to quasi-steady variations in the outflow underneath the dam. A linear stability analysis of the model reveals a multitude of unstable modes and highlights the coupling mechanism that generates the instability. Experiments designed to mimic the theory also found the system to be unstable, and the dominant frequencies of the observed oscillations show satisfying agreement with those predicted to be the most unstable from the linear theory.

Our theoretical study has been limited to an exploration of steady states and their linear stability, however, and we have not made any systematic study of the nonlinear dynamics of the unstable seiches. From a mathematical perspective, the great variety of unstable modes suggests an interesting nonlinear dynamics problem surrounding modal competition. The oscillations observed in the experiments also show definite evidence of nonlinearity, and the smooth amplitude variations seen in figure 12, in particular, are something that one might hope to understand by studying the nonlinear behaviour of the model. The potential complications introduced by momentary closures of the outflow channel due to impacts of the dam with the bottom provide an interesting additional nonlinearity, and in some cases (figure 14*b*) may exert limiting control on the oscillation amplitude.

There are two notable deficiencies of our model, both connected to classical problems in fluid mechanics. The first concerns how flow separates from the downstream edge of the dam, a problem with a rich history in studies of the flow under sluice gates and from the nozzles of jets (e.g. Benjamin 1955). The separation conditions determine how the dam height is related to the downstream water depth, and we swept all the details into an unknown contraction ratio. The second difficulty is in matching the dam region with the upstream shallow water flow in the reservoir. Binder & Vanden-Broeck (2005) suggest that it is not possible to effect such a match, and that the obstacle necessarily generates short-wavelength oscillations upstream. The dynamical effect of such undulations on the larger-scale seiche dynamics is not clear, although there was no visible evidence for them in the experiments. In any case, there does not appear to be a clear way to counter either difficulty without significantly complicating the model.

On the experimental side, we studied only a limited range of the full parameter space, and a more complete exploration may be worthwhile. For example, in none of the experiments reported in this study was there any suggestion that the steady equilibrium state could be stable. The theory, however, does suggest that there may be windows of stability. In a different set of experiments with steeper dams to those explored here (Scolan 2009), there were indications that the system could have stable steady flows, and even be bistable, with sloshing states co-existing with steady equilibria.

It is also worth mentioning that the particular geometry of the reservoir considered in this study is not crucial to the instability mechanism. In fact, we first observed the same type of oscillation in a shallow, triangular-shaped reservoir dammed by a mobile plate on an inclined ramp (Hewitt, Balmforth & McElwaine 2011). Indeed, the general features ought to apply whenever a seiche is able to couple to a movable dam. The instability mechanism relies on a suitable tuning between the dam oscillations and the natural modes of the reservoir, and there is no obvious reason why it would not apply to reservoirs with any shape or depth.

This work was partly conducted at the 2009 Geophysical Fluid Dynamics Summer Program, Woods Hole Oceanographic Institution, which is supported by the National Science Foundation and the Office of Naval Research. I.J.H. acknowledges the support of a Killam postdoctoral research fellowship.

Appendix A. Accounting for the pendulum effect on the moment

In the main text, we defined M as the moment experienced by the dam when it rests on the bottom of the reservoir (i.e. when $h_T = 0$, or $\theta = \theta_0$), but noted that it really depends slightly on the dam's position. The moment can be thought of as that due to a weight acting at the centre of mass of the whole pivoted assembly. As the dam moves up and down, and the assembly rotates, the component of gravity acting as a moment also changes. The moment acting on the dam at any instant therefore has a small dependence on θ , and since $\theta - \theta_0 \ll 1$ this can be approximated as a linear dependence on h_T :

$$\hat{M}(h_T) = M + Ch_T, \quad (\text{A } 1)$$

where C is a small positive constant. In the experiment, C can be estimated by adding a small counterbalancing mass and measuring the change to the equilibrium position h_T (i.e. the position at which $\hat{M} = 0$) without any water flowing.

The experimental data for the steady state depths are plotted in figure 11 as a function of M . Given the steady state measurements of h_T , however, we can use (A 1) to correct for the *actual* moment on the dam, \hat{M} , given the observed position. The actual moment is always larger than M , and the effect is to shift the data at low moments much closer to the theoretical curve.

Appendix B. Accounting for flow around the sides of the dam

The mass conservation equation (2.6) can be modified to allow for the fact that part of the flux, q_L , arriving at the location of the dam from upstream is diverted through the gaps at the sides. If the gaps have a total width W_G , the appropriate modification is

$$q_L = h_L u_L = h_E u_E + \lambda q_G, \quad (\text{B } 1)$$

where $\lambda = W_G/W$ (W is the width of the reservoir) and q_G is the two-dimensional flux through the gaps. A similar modification must be applied to the momentum balance in (2.7), giving

$$F_n \cos \alpha = \frac{W}{\tan \alpha} \left[\frac{1}{2} \rho g (h_L^2 - h_E^2) + \rho h_L u_L^2 - \rho h_E u_E^2 - \lambda \mathcal{M}_G \right], \quad (\text{B } 2)$$

where \mathcal{M}_G is the two-dimensional momentum flux carried by the flow through the gaps. The third ingredient of the model for the dam flow, (2.8), remains unaltered, so

we still have

$$u_E = [2g(h_L - h_E) + u_L^2]^{1/2}. \quad (\text{B } 3)$$

To calculate q_G and \mathcal{M}_G , we suppose that the fluid escaping around the sides, once it flows past the dam, occupies narrow sheets with speed $u_G(z)$. The flux q_G is then given by

$$q_G = \int_{h_E}^{h_L} u_G \, dz. \quad (\text{B } 4)$$

The outflow speed, u_G , depends upon z due to the hydrostatic pressure behind the dam which drives it through. Since the water sheets are in contact with the air as soon as they pass the dam, the downstream pressure is zero, and by applying Bernoulli's principle along the streamlines following the walls,

$$\frac{p}{\rho} + \frac{1}{2}u^2 = g(h_L - z) + \frac{1}{2}u_L^2 = \frac{1}{2}u_G^2. \quad (\text{B } 5)$$

Substituting this expression into (B 4) gives

$$q_G = \int_{h_E}^{h_L} [2g(h_L - z) + u_L^2]^{1/2} \, dz = \frac{1}{3g} \{ [2g(h_L - h_E) + u_L^2]^{3/2} - u_L^3 \} = \frac{u_E^3 - u_L^3}{3g}, \quad (\text{B } 6)$$

using (B 3). The momentum loss in (B 2) can similarly be expressed as

$$\mathcal{M}_G = \int_{h_E}^{h_L} \rho u_G^2 \, dz = \rho g(h_L - h_E)^2 + \rho(h_L - h_E)u_L^2. \quad (\text{B } 7)$$

With these expressions for q_G and \mathcal{M}_G , (B 1) and (B 3) now provide the algebraic relationships needed to express the force F_n as a function of h_L and h_E (as in (2.11) for the purely two-dimensional theory). For the steady states, although the expression for force balance is then less transparent than before, it is straightforward to solve for h_L and h_T , given $q_L = Q$ (again making the assumption $h_E = \mu h_T$).

The predicted steady states are shown in figure 11, where they are plotted against the moment M as corrected for by (A 1). At the lowest moments, the effect of the flow around the sides is negligible and the difference between the original theory (solid line) and the modified one (dashed line) displays the effect of the moment adjustment described in Appendix A. For larger moments, however, the side leakage is more important because although λ is small, when the flux q_L in (B 1) is also small the mass loss q_G can become significant (the momentum loss in (B 2), on the other hand, always remains relatively unimportant). In the dimensionless formulation of §2.7, this situation corresponds to $\Theta \ll 1$, for which the dimensionless h_T and u_L are $O(\Theta)$. The equilibrium state is then given, to leading order in Θ , by

$$1 = \frac{1}{2}H_L^2 - \lambda H_L^2, \quad (\text{B } 8)$$

$$U_T = 2^{1/2}H_L^{1/2}, \quad (\text{B } 9)$$

$$\Theta = H_L U_L = H_T U_T + \lambda \frac{2^{3/2}}{3} H_L^{3/2}, \quad (\text{B } 10)$$

(coming from the scaled (B 2), (B 3) and (B 1), respectively, with U_T the dimensionless steady state exit velocity). From these relations, it is clear that H_L remains largely unaltered by the side leakage (the water must still rise to the same height in order for

the pressure to provide the required force on the dam), but H_T is reduced as more of the water is diverted around the sides:

$$H_T = \frac{1}{2^{3/4}}\Theta - \frac{2^{3/2}}{3}\lambda, \quad (\text{B } 11)$$

to leading order in Θ and λ . Note that this also predicts that the dam rests on the bottom, with all the flow passing through the gaps at the sides, if $\Theta \leq 2^{9/4}\lambda/3$.

REFERENCES

- ARGENTINA, M. & MAHADEVAN, L. 2005 Fluid-flow-induced flutter of a flag. *Proc. Natl. Acad. Sci. USA* **102**, 1829–1834.
- BACKUS, J. 1961 Vibrations of the reed and the air column in the clarinet. *J. Acoust. Soc. Am.* **33**, 806–809.
- BACKUS, J. 1963 Small-vibration theory of the clarinet. *J. Acoust. Soc. Am.* **35**, 305–313.
- BAKKER, A. D., JONGELING, T. H. G., KOLKMAN, P. A. & WU, Y. S. 1991 Self-excited oscillations of a floating gate related to the gate discharge characteristics. Delft Hydraulics, Publication 462.
- BATCHELOR, G. 1967 *An Introduction to Fluid Mechanics*. Cambridge University Press.
- BENJAMIN, T. B. 1955 On the flow in channels when rigid obstacles are placed in the stream. *J. Fluid Mech.* **1**, 227–248.
- BENJAMIN, T. B. 1960 Effects of a flexible boundary on hydrodynamic instability. *J. Fluid Mech.* **9**, 513–532.
- BILLETER, P. & STAUBLI, T. 2000 Flow-induced multiple-mode vibrations of gates with submerged discharge. *J. Fluids Struct.* **14**, 323–338.
- BINDER, B. J. & VANDEN-BROECK, J.-M. 2005 Free surface flows past surfboards and sluice gates. *Euro. J. Appl. Math.* **16**, 601–619.
- FITT, A. D. & POPE, M. P. 2000 The unsteady motion of two-dimensional flags with bending stiffness. *J. Engng Math.* **40**, 227–248.
- HARDWICK, J. D. 1974 Flow-induced vibrations of vertical-lift gate. *ASCE J. Hydraul. Div.* **100**, 631–644.
- HELMHOLTZ, H. 1954 *On the Sensations of Tone*. Dover.
- HEWITT, I. J., BALMFORTH, N. J. & MCELWAINE, J. N. 2011 Continual skipping on water. *J. Fluid Mech.* **669**, 328–353, doi:10.1017/S002211201000050.
- JONGELING, T. H. G. & KOLKMAN, P. A. 1995 Subharmonic standing cross waves leading to low-frequency resonance of a submersible flap-gate barrier. Delft Hydraulics, Publication 490.
- JULIAN, B. 1994 Volcanic tremor: nonlinear excitation by fluid flow. *J. Geophys. Res.* **99**, 11859–11877.
- KOLKMAN, P. A. 1977 Self-exciting gate vibration. In *Proceedings of the 17th Congress of the International Association for Hydraulic Research*. vol. 4, pp. 372–381.
- KUELEGAN, G. H. 1959 Energy dissipation in standing waves in rectangular basins. *J. Fluid Mech.* **6**, 33–50.
- LANDAHL, M. 1962 On the stability of a laminar incompressible boundary layer over a flexible surface. *J. Fluid Mech.* **13**, 607–632.
- MANDRE, S. & MAHADEVAN, L. 2009 A generalized theory of viscous and inviscid flutter. *Proc. R. Soc. Lond. A* **466**, 141–156.
- MCINTYRE, M. E., SCHUMACHER, R. T. & WOODHOUSE, J. 1983 On the oscillations of musical instruments. *J. Acoust. Soc. Am.* **74**, 1325–1345.
- MISRA, A., BEHDINAN, K. & CLEGHORN, W. L. 2002 Self-excited vibration of a control valve due to fluid–structure interaction. *J. Fluid Struct.* **16**, 649–665.
- MÜLLER, C., SCHLINDWEIN, V., ECKSTALLER, A. & MILLER, H. 2005 Singing icebergs. *Science* **310**, 1299.
- RUST, A., BALMFORTH, N. J. & MANDRE, S. 2008 The feasibility of generating low frequency volcano seismicity by flow through a deformable channel. In *Fluid Motions in Volcanic Conduits; A Source of Seismic and Acoustic Signals* (ed. S. J. Lane and J. S. Gilbert) *London Geological Society, Special Publications*, vol. 307, pp. 45–56.

- SCOLAN, H. 2009 Flow-destabilized seiche modes with a movable dam. *2009 GFD Summer School Rep.* Woods Hole.
- WEAVER, D. S. & ZIADA, S. 1980 A theoretical model for self-excited vibrations in hydraulic gates, valves and seals. *Trans. ASME* **102**, 146–151.
- WILSON, T. A. & BEAVERS, G. S. 1974 Operating modes of the clarinet *J. Acoust. Soc. Am.* **56**, 653–658.